Journal of
Composites Science

MDPI

Article

Molecular Dynamics Assessment of Mechanical Properties of Fullerphene and Fullerphene/Graphene Composite

Mingjun Han [1,2], Taotao Yu [1,2], Yinghe Zhang [1,2], Xue Chen [3], Xiao-Jia Chen [1], Qing Peng [1,3,4,*] and Ho-Kin Tang [1,2,*]

1 School of Science, Harbin Institute of Technology (Shenzhen), Shenzhen 518055, China
2 Shenzhen Key Laboratory of Advanced Functional Carbon Materials Research and Comprehensive Application, Harbin Institute of Technology (Shenzhen), Shenzhen 518055, China
3 State Key Laboratory of Nonlinear Mechanics, Institute of Mechanics, Chinese Academy of Sciences, Beijing 100190, China
4 Guangdong Aerospace Research Academy, Guangzhou 511458, China
* Correspondence: pengqing@imech.ac.cn (Q.P.); denghaojian@hit.edu.cn (H.-K.T.)

Abstract: Quasi-hexagonal-phase fullerene ($qHPC_{60}$) is an asymmetrically ordered arrangement of fullerene in the two-dimensional plane, which has been synthesized recently. In this study, we performed a comprehensive investigation of the anisotropic mechanical properties of a $qHPC_{60}$/graphene composite by means of molecular dynamics simulations. We assessed the mechanical properties of the 2D torsion-angle fullerene model with three force-fields: AIREBO, REAXFF, and TERSOFF. The results of the uniaxial tensile tests show that while the variations in fracture stress and fracture strain, with respect to pre-crack size, had similar trends for the three force-fields, AIREBO was more sensitive than REAXFF. The presence of cracks degraded the mechanical properties. Simulations of tensile tests on the $qHPC_{60}$/graphene composite revealed that the graphene substrate significantly increased mechanical strength. Our results suggest $qHPC_{60}$ holds various promising implications for composites.

Keywords: monolayer fullerene; fracture behavior; molecular dynamics simulation; tensile property; pre-crack system; graphene substrate

Citation: Han, M.; Yu, T.; Zhang, Y.; Chen, X.; Chen, X.-J.; Peng, Q.; Tang, H.-K. Molecular Dynamics Assessment of Mechanical Properties of Fullerphene and Fullerphene/Graphene Composite. *J. Compos. Sci.* **2024**, *8*, 310. https://doi.org/10.3390/jcs8080310

Academic Editor: Traian Dumitrica

Received: 1 July 2024
Revised: 30 July 2024
Accepted: 6 August 2024
Published: 8 August 2024

1. Introduction

Compared to bulk-phase materials, monolayer 2D materials have ultimately small thickness levels and a high surface ratio. The energy band structure and electrical properties can be more easily tuned by thickness control and elemental doping, thus demonstrating great potential for application in different areas, such as sensors, catalysis, batteries, biomedicine, and so on. Graphene [1] (GE), a typical 2D material, is widely used in electronics and optoelectronics due to its high mechanical strength, flexibility, and electrical conductivity. However, its zero-bandgap property limits its application in traditional semiconductor fields [1–3]. The structural stability and electronic properties of another typical material, 2D fullerphene, are also of great interest.

Fullerene C_{60} processes excellent properties and has a wide range of applications in thermoelectric fields, optoelectronic devices, and medicine, etc. The study of the physical properties of C_{60} and its derivatives also plays a crucial role in their practical applications. Many studies on the mechanical properties and thermal stability of $qHPC_{60}$ and $qTPC_{60}$ have been carried out. Tromer et al. [4] found that $qHPC_{60}$ has a moderate direct electronic band gap and anisotropic mechanical properties and can act as a UV collector of photon energy up to 5.5 eV. Yu et al. [5] proposed three bridged fullerene monolayers and comprehensively investigated the experimentally synthesized novel fullerene monolayer (α-C_{60}-2D) by state-of-the-art first-principles computational methods, measuring

its anisotropic Young's modulus and Seebeck coefficient at low and intermediate temperatures. Peng [6] employed semilocal density functional theory and hybrid functional calculations to investigate the electronic structures of monolayer fullerene networks. They concluded that all the phases of monolayer fullerene networks have suitable band gaps with high carrier mobility and appropriate band edges to thermodynamically drive overall water splitting. Dong et al. constructed an accurate and transferable machine learning potential to study the heat transfer and related properties of $qHPC_{60}$ and compared it to face-centered cubic-phase fullerene (BPC_{60}). Using homogeneous nonequilibrium molecular dynamics and correlation spectral decomposition methods, it was shown that the thermal conductivity of $qHPC_{60}$ is anisotropic [7]. Yuan et al. [8] systematically investigated the electronic structure and optical properties of monolayer $qHPC_{60}$ and mono-layer $qTPC_{60}$ using first-principles calculations.

Regarding mechanical properties, Ying et al. [9] comprehensively investigated the properties of newly synthesized monolayer $qHPC_{60}$ films under axial tension by using density-functional theory (DFT) calculations and molecular dynamics (MD) simulations combined with a machine-learning neural network potential. The elastic and fracture behavior of monolayer $qHPC_{60}$ was found to be strongly anisotropic. In addition, machine learning interatomic potentials have been used to investigate the mechanical and thermal properties of various nanosheet phases, including C_{60} and C_{36} [10,11], and the method can be used to explore the acoustic properties, thermal conductivity, and mechanical response of nanomaterials [12–15]. Peng [16] performed a detailed DFT study to compare the mechanical, kinetic, or thermodynamic stability of $qTPC_{60}$ and $qHPC_{60}$. Yu et al. [17] computationally investigated the enhancement of the mechanical stability of 2D fullerenes by the encapsulation and addition of graphene substrates. Zhao et al. [18] found that the ultimate tensile strength and the work of rupture of the monolayer $qHPC_{60}$ reached a maximum at 15° and 75°, respectively, as determined by a DFT study. Shen et al. [19] computationally investigated the thermal, structural, mechanical, and thermomechanical stability, as well as the adhesion, ductility and mechanical properties, of $qHPC_{60}$. Ribeiro et al. [20] calculated the thermomechanical stability and fracture modes of $qHPC_{60}$ and $qTPC_{60}$ by MD. The results showed that these structures have similar thermal stability with sublimation points of 3898 K and 3965 K. $qTPC_{60}$ undergoes a sudden structural change after the critical strain threshold and breaks completely. $qHPC_{60}$ ($qTPC_{60}$) has a linear (nonlinear) crack growth. $qHPC_{60}$ and $qTPC_{60}$ have an estimated elastic modulus of 175.9 GPa and 100.7 GPa, respectively; the DFT method is accurate but does not allow for film size and finite temperatures.

All the aforementioned atomistic investigations are carried out in relatively small simulation boxes, which in turn exclude some long-range interactions. A larger model is lacking to check the influence of the size effect on the mechanical properties. Furthermore, there are considerable discrepancies among the atomistic studies, mainly due to the different descriptions of the interatomic interactions. A comprehensive comparison of the mechanical properties is missing. Anisotropic fracture failure behaviors are crucial in engineering applications. Although a DFT study shed light on it [18], its behaviors at finite temperatures is still elusive. In addition, the mechanics of a composite formed by one $qHPC_{60}$ monolayer and one graphene monolayer are unsettled.

In this paper, we investigate the mechanical properties of the larger-scale $qHPC_{60}$ system via large MD simulations, complementing the gap in this research. We assess the anisotropic mechanical properties of the system under different potential function descriptions (including REAXFF, AIREBO, and TERSOFF potentials) and measure the fracture strain and fracture stress of the system at a fixed temperature. In addition, the use of graphene/fullerphene/graphene intercalation has been proposed, demonstrating that the interfacial thermal resistance can show a switchable step change by varying the amount of fullerenes in the intercalation structure [21]. We will also investigate the mechanical properties of the fullerphene/graphene intercalation and probe the effects caused by defects and cracks.

The discussion of these is divided into three sections. Section 2 provides a detailed overview of the methods used in this study, including computational techniques and parameters. In Section 3, we investigate the effect of different factors on the mechanical properties of C_{60}. This includes stretching in different directions and the description of the system by different potential functions.

2. Materials and Methods

Molecular dynamics simulations were employed using the software package LAMMPS Stable Release (2 August 2023) (large-scale atomic/molecular massively parallel simulator) [22]. OVITO (open visualization tool) [23] was used to analyze atomic simulation results and graphs. Adaptive Intermolecular Reaction Bond Order (AIREBO) [24] and Reactive Force Field (REAXFF) [25] were chosen as the force fields capable of describing the inter-atomic interactions between carbon atoms. AIREBO potential was modified for carbon nanostructures with significant deformation [26]. The simulation model is a two-dimensional fullerene supercell, and the scale of the model is controlled to be around 10,000 atoms in order to improve the computational efficiency and shorten the simulation time. The simulated tensile process adopts periodic boundary conditions, and the simulation step size is set to 1 fs. Firstly, the simulated system is subjected to 2000 ps structural relaxation under the NPT system so as to minimize the energy of the system and eliminate the influence of the internal stresses of the model on the simulation results; then, the load is applied to the x-direction to carry out the tensile deformation operation for 5000 ps; the system force is calculated by 100 samples for every 1 ps and time averaging; and finally, the stress–strain curve is plotted, and the position of atoms are output. Then, the load is applied in the x direction, and the tensile deformation is carried out for 5000 ps; 100 samples are taken every 1 ps, and time is averaged to calculate the force applied to the system. Since the TERSOFF potential function [27] does not describe the stretched system well, we do not discuss it in the main text; the relevant information is given in the appendix.

The original cell of 2D $qHPC_{60}$ contains 60 carbon atoms. As shown in Figure 1, we converted the orthorhombic cell into monoclinic cells with different angles and performed supercell expansion on them. Two types of fullerenes interbond exist in $qHPC_{60}$, with covalent [2 + 2] cycloaddition bonds along the [010] direction and C-C single bonds along the [110] and [110] directions. All simulations were carried out at 300 K and the stretching direction along the positive x-axis. The direction of the arrow in Figure 1 indicates the direction of stretching. The bond angles and bond lengths remain essentially unchanged in the torsion-angle model compared to the original model. Due to the difference in the arrangement of double and single bonds, the torsion-angle models with different orientations will exhibit mechanical properties of different strengths during the stretching process.

The AIREBO [24] and REAXFF potentials chosen for the simulation are based on the idea of bond order (BO), which takes into account covalent bond breaking and formation [28]. The AIREBO potential is often used to study high-temperature reaction processes and the mechanical properties and elasticity of carbon nanostructures at room temperature. It is based on Brenner's reactive empirical bond-order potential REBO, with additional consideration of torsional and long-range non-bonding interactions. The REAXFF potential is another generic potential dependent on bond order that uses the relationship between bond distance and bond order, on the one hand, and the relationship between bond order and bond energy, on the other hand, to realistically describe bond formation and dissociation, and it is excellent for describing chemical reactions in multi-element simulations. Depending on the specific parameter settings, the functionality can go far beyond carbonaceous systems. The potential contains the over-coordination term E_{over} to avoid unrealistically high bond-order values on the atoms and specifically describes system-specific interatomic interactions. Its bond-order resolvent is more complex compared to the AIREBO.

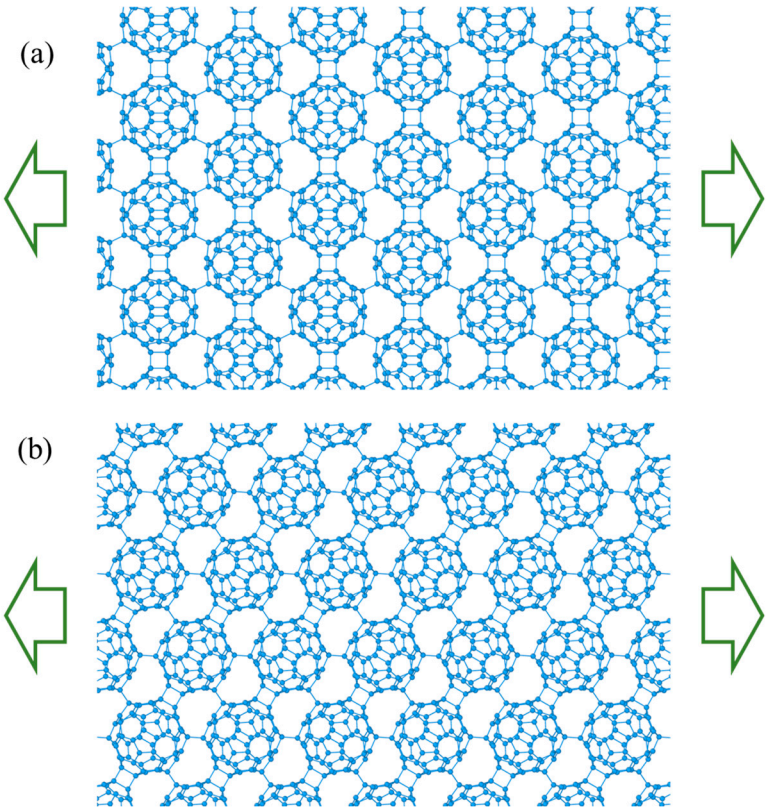

Figure 1. Monolayer fullerphene, (**a**) 0° torsion-angle model, (**b**) 30° torsion-angle model.

A new potential function for carbon condensed phases, called REAXFF$_{C2013}$ [29], which contains the heat of the deformation of graphite, the heat of the formation of Stone–Wales defects in graphene, and the heat of the formation of some amorphous carbon phases, was obtained during the simulated thermal decomposition of fullerenes in the parametric training set of the potential and it explicitly clarified the various parameters of the potential based on the first-principles calculations.

An important difference between the REAXFF model and the AIREBO model is that REAXFF uses a much longer range of exponentially decaying BO/bond distance relations without any cut-off value. The modified AIREBO potential (R_{min} = 2 Å) can give reasonable results compared with experimental results. The REAXFF potential additionally takes into account non-bonding interaction forces, which are more comprehensively considered compared to AIREBO's potential; therefore it is considered to be, possibly, a relatively more accurate potential function [30].

Fracture stress is derived from tensile simulation and is defined as the peak stress in the stress–strain curve since it is brittle. The fracture strain is the corresponding strain of the fracture stress.

3. Results and Discussion

3.1. Stretching the Torsion-Angle Model with Different Potential Functions

By twisting different angles, we obtained seven 2D torsion-angle fullerphene models. With the description of different potential functions, we stretched the models uniaxially with the *x*-axis in the 0° direction and the *y*-axis in the 90° direction to obtain the structural stresses and structural strains of the models. Figure 2a shows the stress–strain curves of different torsion-angle models with AIREBO potential function. It can be seen that the fracture stress for the 90° torsion-angle model is the maximum, about 80 GPa, and fracture stress for the 15° torsion-angle model is the minimum, about 15 GPa. The fracture strain of each torsion-angle model is similar, which is about 0.34, and that of the 45° torsion-angle model is slightly larger, which is about 0.37. Figure 2b shows the stress–strain curves of

different torsion-angle models with the potential function of REAXFF; the fracture stress for the 0° torsion-angle model is the maximum, about 25 GPa, and the fracture stress for the 15° torsion-angle model is the minimum, about 5 GPa. The fracture strains for each of the torsion-angle models are similar, which are all around 0.14.

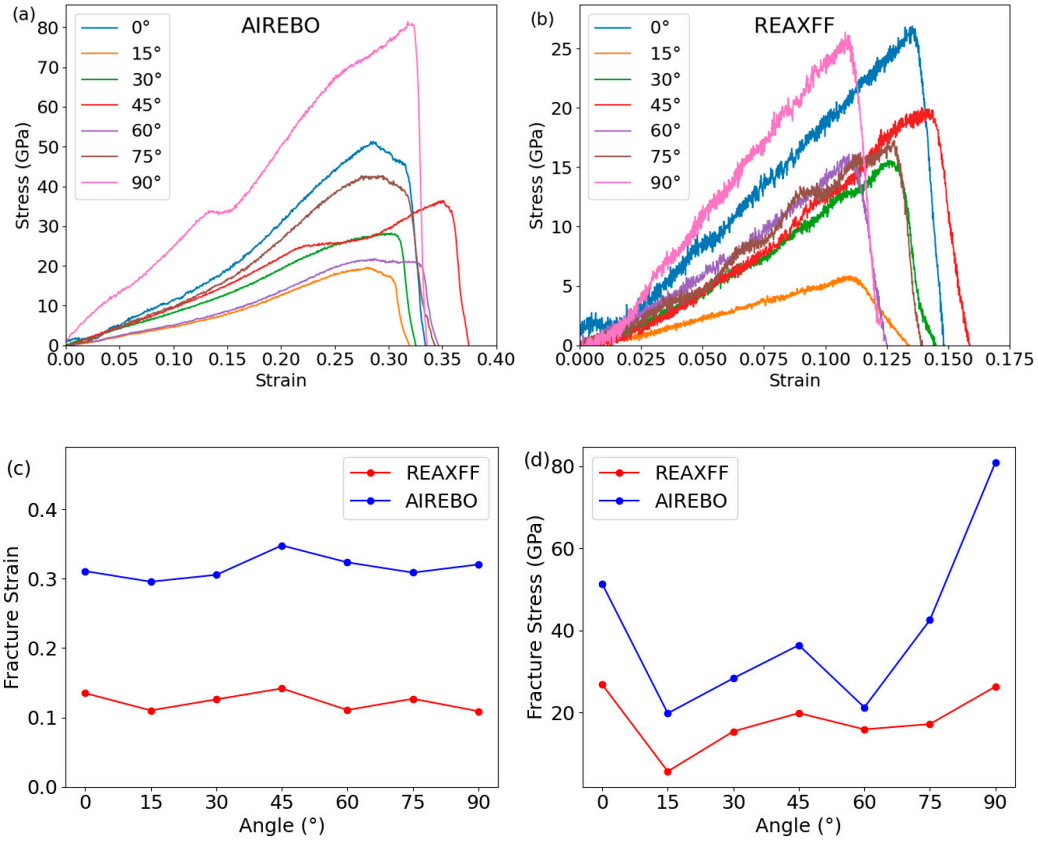

Figure 2. Stress–strain curves of tensile tests with (**a**) AIREBO potential function and (**b**) REAXFF potential function. (**c**) The fracture strain and (**d**) fracture stress in the seven models varied with different tensile angles ranging from 0° to 90°. The red and blue lines are for REAXFF and AIREBO potentials, respectively.

A comparison of the fracture strains with two potential functions is shown in Figure 2c. The fracture strains of the models are overall smaller with the REAXFF potential, which means that the models are more prone to fracture. Comparison of the fracture stresses with the two potential functions is shown in Figure 2d; the overall fracture stress with the AIREBO potential is large, which may be due to the fact that non-bonding interactions were not taken into account. The fracture stresses of the model for the 90° torsion-angle model are particularly prominent, which is probably due to the fact that the strength in this direction is determined by the C=C bonds, while the strength in other directions is governed by weaker C-C bonds.

During stretching, we observe the breaking of chemical bonds. Molecular sphere rupture and possible slight deformations can have an effect on the practical application of the material; in order to study this, we need to focus on the volumetric strain of the material. Volumetric strain is a measure of the extent to which a material or object expands or contracts due to an external force and is defined as the change in the volume of the material divided by the original volume. During the stretching process, the material deforms due to the external force, and the C_{60} molecule gradually changes from a regular sphere to an ellipsoid shape, but the deformation is not obvious due to the stiffness of the C_{60} molecule itself. Here, we have plotted an image of the volumetric strain to show this change. Figure 3

shows the comparison of volumetric strain before and after fracture for each angular model at REAXFF potential.

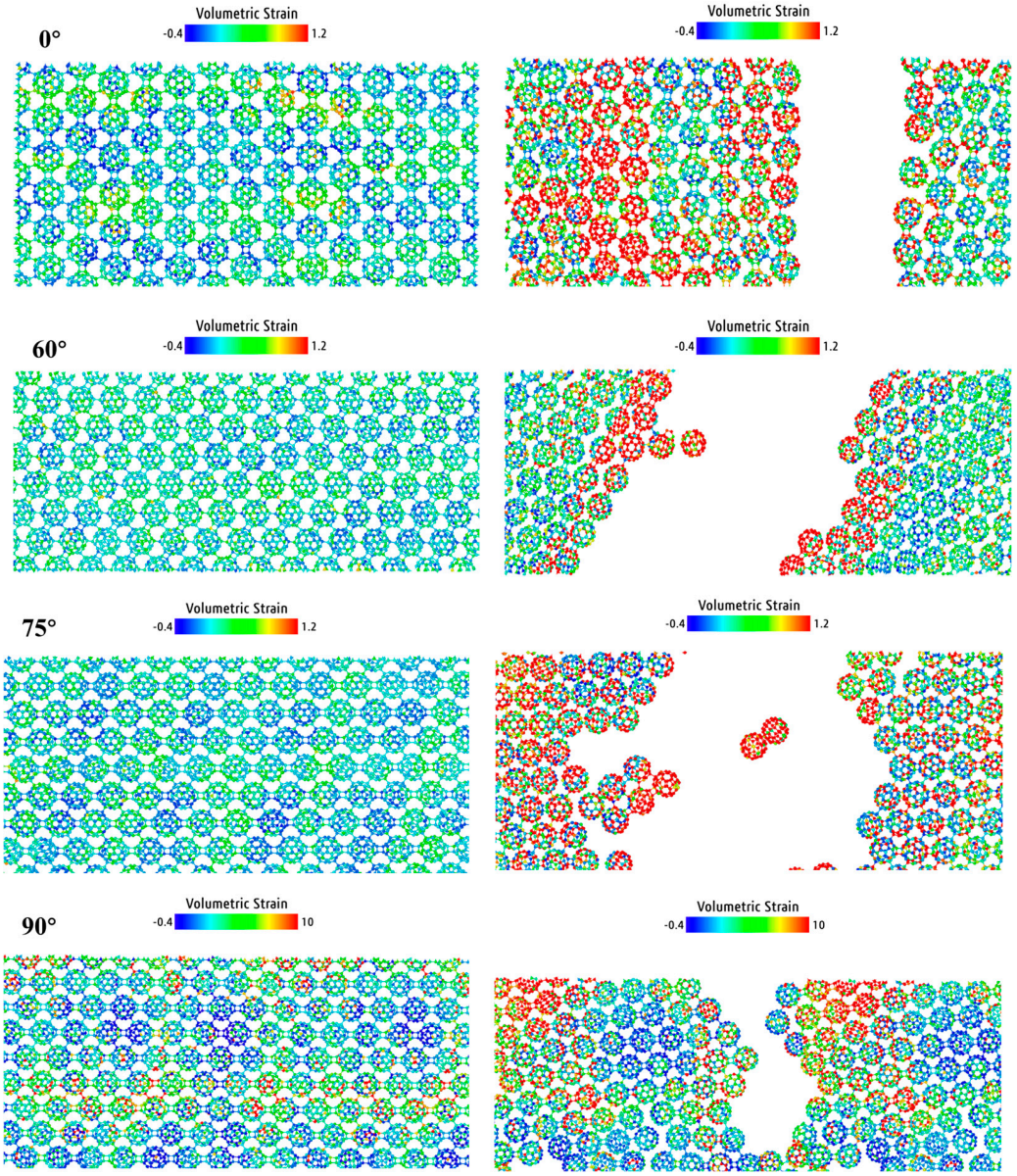

Figure 3. Volumetric strain images before fracture (**left**) and after fracture (**right**) of the seven different models with the torsion-angle from 0° to 90°. The 15°, 30°, and 45° angles are shown in Appendix C.

We chose the frame before fracture of the 0° and 60° models for mechanical analysis. The diagrams of the xx component of the average stress and the xx component of the stretch tensor are displayed in Figure 4, left and right, respectively. It can be observed that the stress is mainly concentrated on the C-C connected between the molecular spheres at the time of fracture, showing a more regular radial distribution, and the stress decreases sharply or disappears when the C-C bond is broken. Deformation of the models mainly occurs at the crack. The deformation of the rest of the model is similar to that of the corresponding model without cracks, which indicates that the C_{60} molecule has a higher hardness and a higher stability.

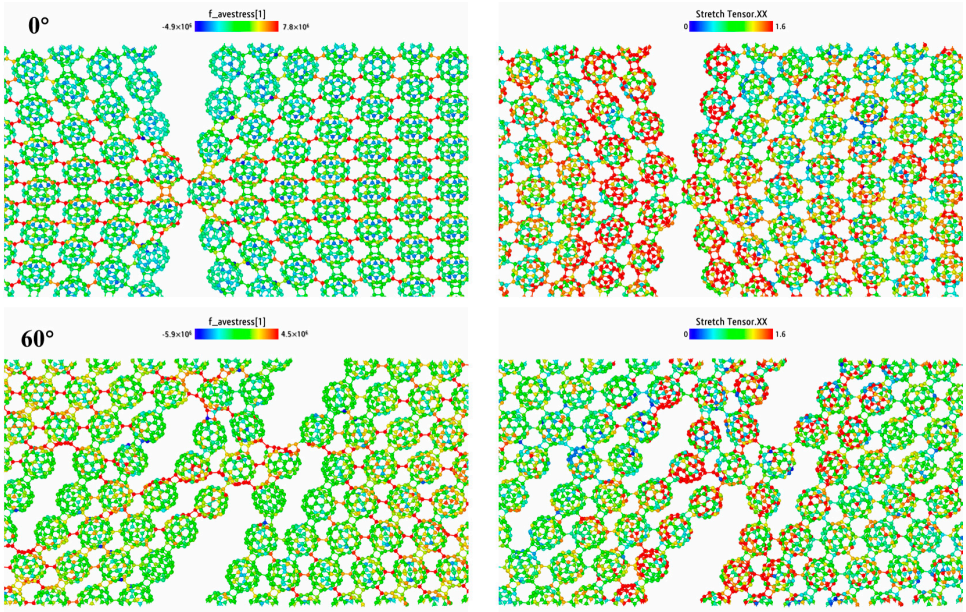

Figure 4. Xx component of the average stress (**left**) and the xx component of the stretch tensor (**right**) for the 0° (**top**) and 60° (**bottom**) models. The corresponding data for the other models are in Appendix C.

Figure 3 shows the comparison of volumetric strain before and after fracture for each angular model at REAXFF potential. Corresponding RDF (radial distribution function) are shown in Figure 5. From Figure 5, one can see that the difference in RDF before and after the fracture of different models is very small. Normalized pair separation distance is defined as the ratio of the distance between a pair of atoms in the deformed state to their distance in the undeformed reference state. This normalization allows for a consistent comparison of separation distances across different deformation states and provides a dimensionless measure of the extent of deformation. Therefore, we arbitrarily chose the model (here, we chose the 60° torsion-angle model) to compare the difference in RDF before and after the fracture of the same model. The RDF of the 60° torsion-angle model after fracture is slightly reduced compared with that before fracture, but the position of the peaks is basically unchanged. This result indicates that the interatomic interactions and the relative positions are unchanged. The crystal structure is stable, and the molecular sphere still retains its original characteristics under stretching; no drastic deformation occurs.

Corresponding distribution histograms (normalized) are shown in Figure 6. Normalized counts are the number of occurrences of a particular volumetric strain value divided by the total number of occurrences of all strain values. This normalization process allows the shape of the distribution to be compared across samples or conditions on a common scale, typically ranging from 0 to 1. To describe the volumetric strain distribution, a histogram of the volumetric strain distribution is plotted. The horizontal axis (x-axis) represents the range of volumetric strain values observed in the samples, while the vertical axis (y-axis) represents the normalized counts, i.e., the frequency of each volumetric strain value normalized by the total number of occurrences. For the distribution of volumetric strain, before fracture, there is a big difference between the different models shown in Figure 6a. The peaks of the 90° torsion-angle model are closer to the left, the peaks of the other models are gradually shifted to the right, and the peaks of the 0° and 60° torsion-angle models are the furthest to the right. This indicates that the 90° torsion-angle model is more prone to be fractured. The strength of the 0° and 60° torsion-angle models is the largest. The strength of the 75° torsion-angle model is in the middle. The statistical distributions of volumetric strain of all models tend to be the same after pulling off, as shown in Figure 6b.

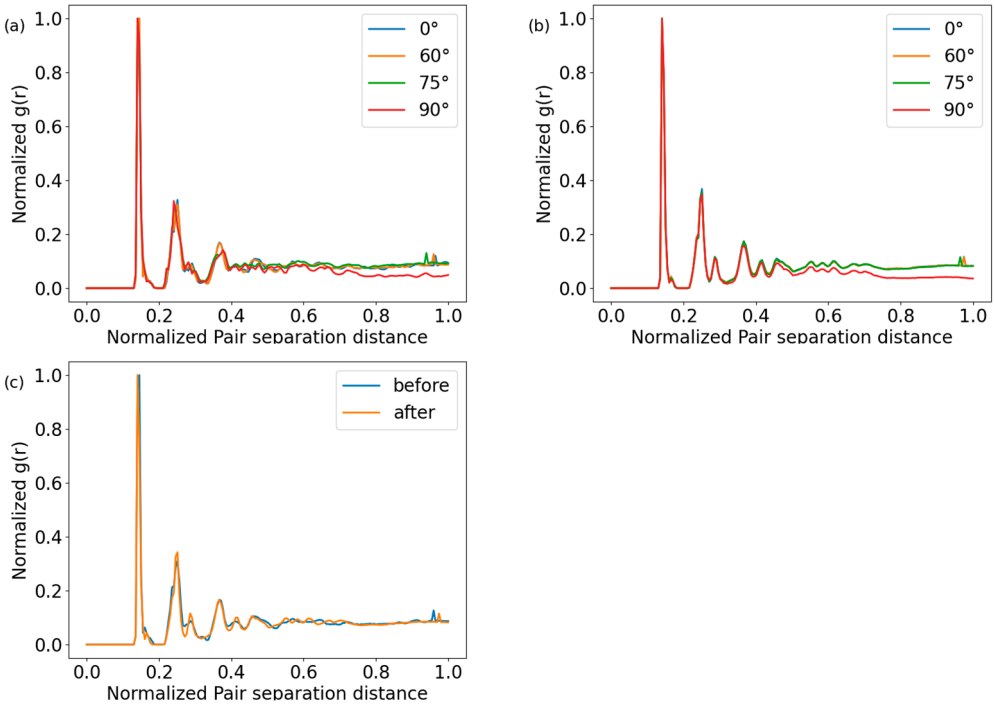

Figure 5. Corresponding RDF (radial distribution function) before (**a**) and after (**b**) fracture; RDF of 60° model (**c**).

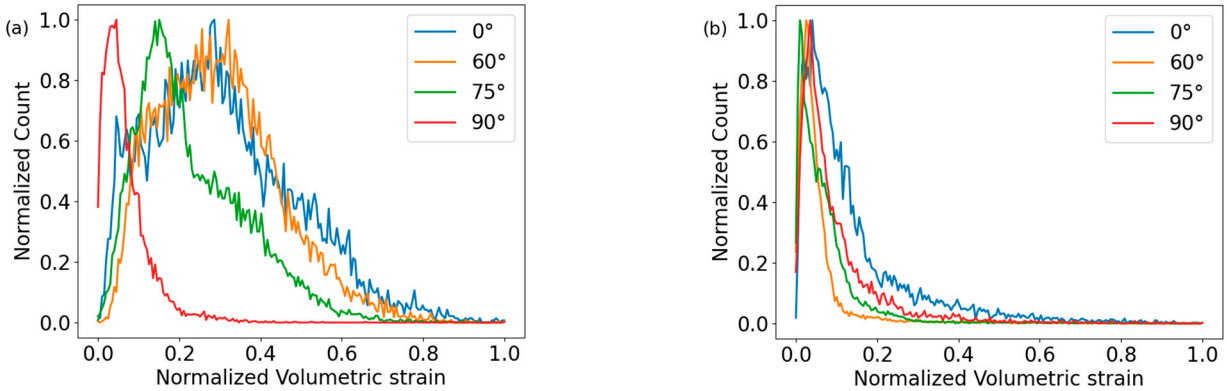

Figure 6. Volumetric strain distribution histograms (normalized) before (**a**) and after (**b**) fracture.

The effect of both changing the size of the model dimensions and the stretching rate on the tensile results have been studied in detail by Yu et al. [17].

3.2. Stretching of GE/qHPC$_{60}$

The tensile study conducted showed that qHPC$_{60}$ is brittle. How to enhance the strength of the material is an explorable question. Previous studies have shown that graphene has higher mechanical strength relative to qHPC$_{60}$ and is less likely to break in tensile experiments [17]. Therefore, we consider adding a graphene substrate to qHPC$_{60}$ in the hope of increasing the mechanical strength of the model. In order to investigate the effect of the addition of graphene substrate on the mechanical properties of the 2D twisted-angle fullerene model, we used Material Studio 2022 for modeling, as shown in Figure 7a, and LAMMPS for tensile testing of the new model, and the tensile curve is shown in Figure 7b and 7c, respectively.

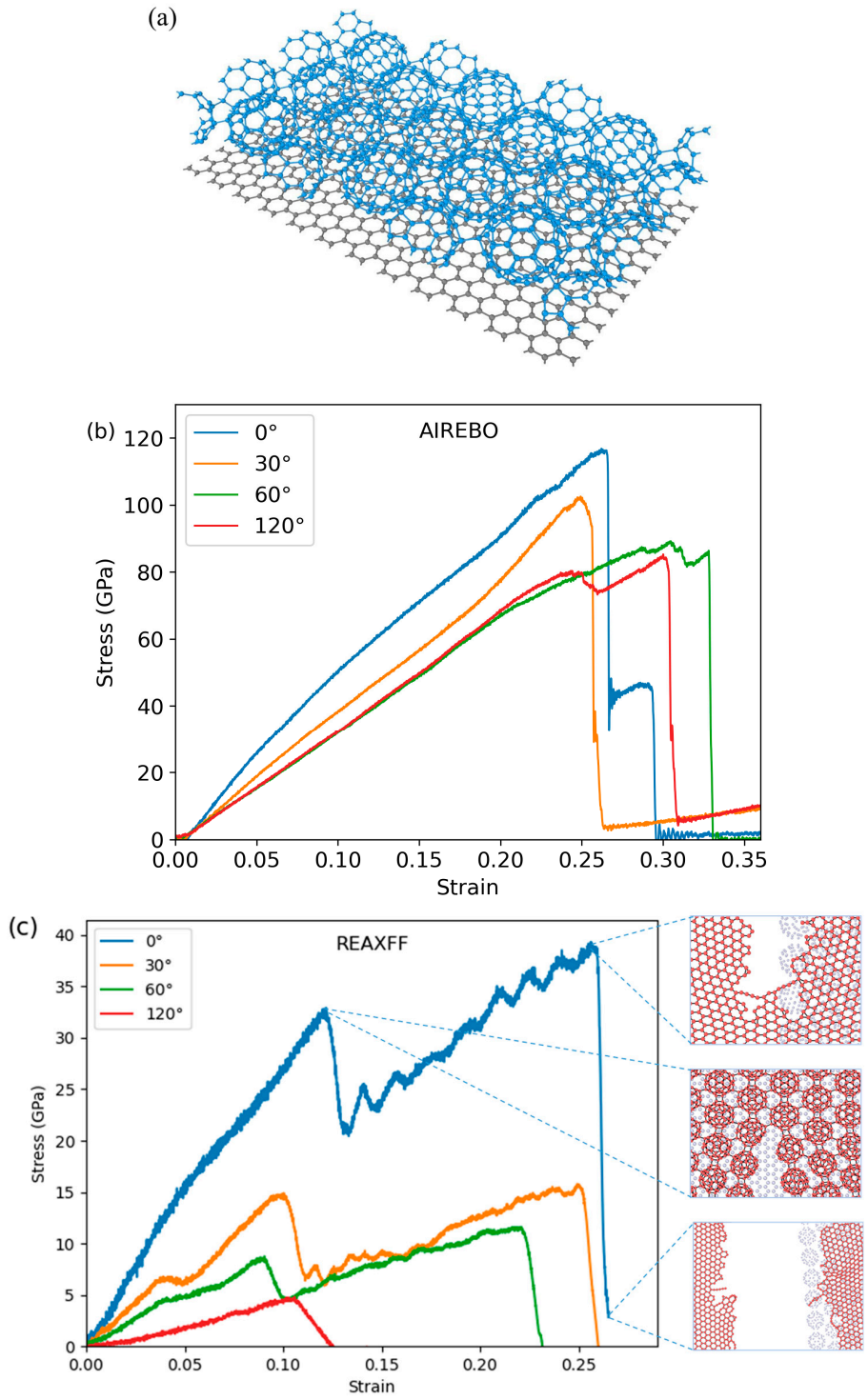

Figure 7. (**a**) Schematic diagram of the model structure. Stress–strain curves for GE/qHPC60 tensile tests under (**b**) AIREBO potential and (**c**) REAXFF potential.

Figure 7b is the stress–strain curve of the torsion-angle model with graphene substrate under the AIREBO potential. The fracture stress for the 0° torsion-angle model is the maximum, which is about 120 GPa. The fracture stress for the 120° torsion-angle model is the minimum, which is about 85 GPa. The fracture strain for the torsion-angle model of each angle is between 0.25 and 0.35. Figure 7c shows the stress–strain curves of the torsion-angle model with graphene substrate under the REAXFF potential. The maximum fracture stress is about 40 GPa for the 0° torsion-angle model. The minimum fracture stress is about 4 GPa for

the 120° torsion-angle model. The fracture strain for the torsion-angle model at each angle is between 0.1 and 0.26. With both potential functions, the curves show a quadratic fracture, indicating that the fracture process of the model is divided into two stages.

In the first stage of fracture, the $qHPC_{60}$ layer is pulled off, and the intermolecular single-bond connection is destroyed. The $qHPC_{60}$ sphere does not undergo large deformation and destruction. As the stretching proceeds, it goes from a tear to a complete fracture. The curve has a sharp drop, at which time the graphene layer remains intact. In the second stage of fracture, the curve ushers in a second drop. The $qHPC_{60}$ layer is completely fractured, and the graphene layer deforms under the stretch. It changes from a square hexagonal shape into a flatter hexagonal shape. When tearing occurs, the C-C bond at the crack is destroyed. The graphene lattice on both sides of the crack is partially and completely deformed, stretched into a one-dimensional chain of atoms, or connected into a ring polygon. As stretching proceeds, the graphene layer is completely fractured. The stress becomes 0. Some of the atoms at the fracture are connected in a chain-like manner. There are no new compounds formed when the model breaks during stretching.

In the study of graphene-based composites, the effect of vacancy defects is a significant and worthwhile issue to explore in depth. Vacancy defects can substantially alter the mechanical properties of the material, making it crucial to understand their mechanisms to optimize material design. In this study, we created a rectangular vacancy defect with a length of 5 Å and a width of 20 Å in the central region of the aforementioned GE/qHPC60 material. We then conducted uniaxial tensile simulations of the material in the x-direction using the AIREBO potential function to investigate the impact of the vacancy defect on the material's mechanical properties.

The experimental results presented in Figure 8 demonstrate that the vacancy defect significantly affects the mechanical response of different corner models. The fracture stress and fracture strain were notably reduced for all corner models, with the highest peak stress at a strain of approximately 0.09, ranging from 10 GPa to 27 GPa. This range is substantially lower compared to the peak stress observed in the absence of vacancies. To further verify this finding, we also performed tensile simulations under the same conditions using the TERSOFF potential function (see Appendix A). Comparing the simulation results of the two potential functions, we found that despite differences in exact values, both indicate that vacancy defects lead to a significant decrease in the mechanical properties of the material.

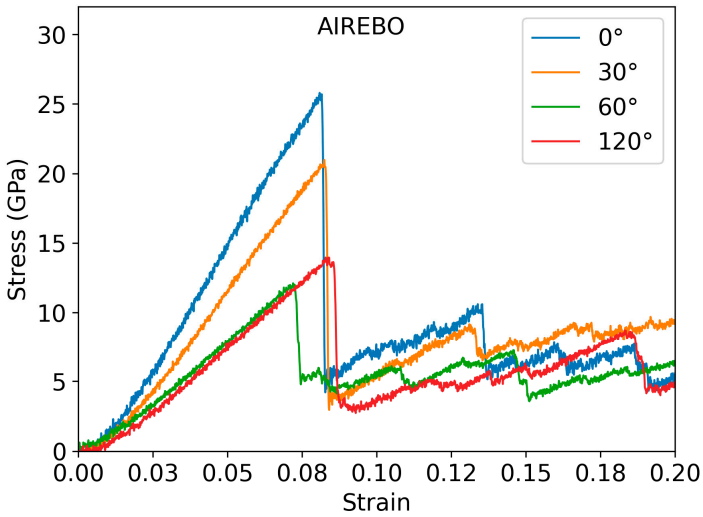

Figure 8. Stress–strain curves from tensile tests using the AIREBO potential function for the GE/qHPC60 system with vacancies.

3.3. Stretching qHPC60 with Single Vacancy

In order to investigate the effect of the single vacancy on the mechanical properties of the torsion-angle model, we removed an intact C_{60} molecule from the original model, as

shown in Figure 9a, and performed tensile tests on the new model. The experiments show that the single vacancy reduces the fracture stress of the model. Interestingly, we observed tearing in the tensile test, as shown in Figure 9b. The picture shows the tensile process of the 75° torsion-angle model with the AIREBO potential. Under the action of tensile force, the model is first torn through a large crack, and the single-bond connection between atoms becomes atomic-chain connection, at which time the stress curve shows a large drop but not 0. Under the action of continuous stretching, the atomic chain is completely broken, the stress curve again drops sharply, and the stress becomes 0.

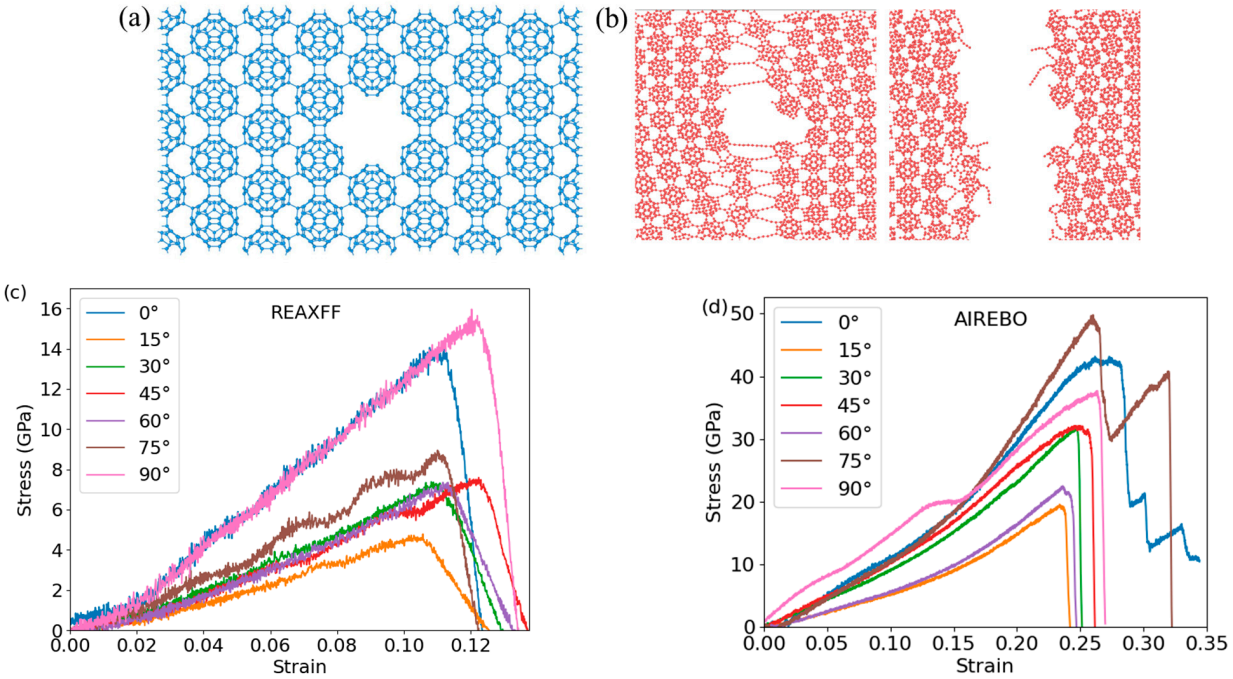

Figure 9. (**a**) Schematic diagram of the model structure. (**b**) The tearing that occurs when the model is stretched out. (**c**,**d**) Stress–strain curves for model tensile tests under AIREBO potential and REAXFF potential.

To compare the effect of cracks on the mechanical strength of the models with different potential functions, we plotted the fracture stress and strain curves with and without cracks for each torsion-angle model, as shown in Figure 10. This Figure shows that the fracture strain of the model without cracks is significantly higher than that of the model with cracks for both REAXFF and AIREBO potentials. Overall, the metrics for the AIREBO potential function are higher than those for the REAXFF potential. However, the REAXFF potential is expected to present more accurate results due to its consideration of non-bonding interactions.

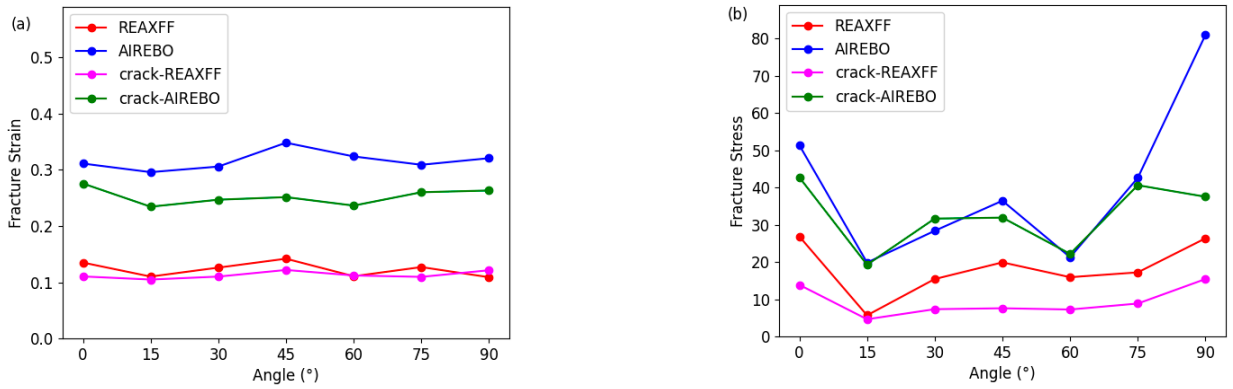

Figure 10. (**a**) Fracture strain and (**b**) fracture stress of each model.

In this paper, we focus on the stress–strain curves for the tensile simulations of each system. In order to highlight the anisotropy of the material, we also investigated Young's modulus. Correspondence with the torsion angle is shown in Figure 11.

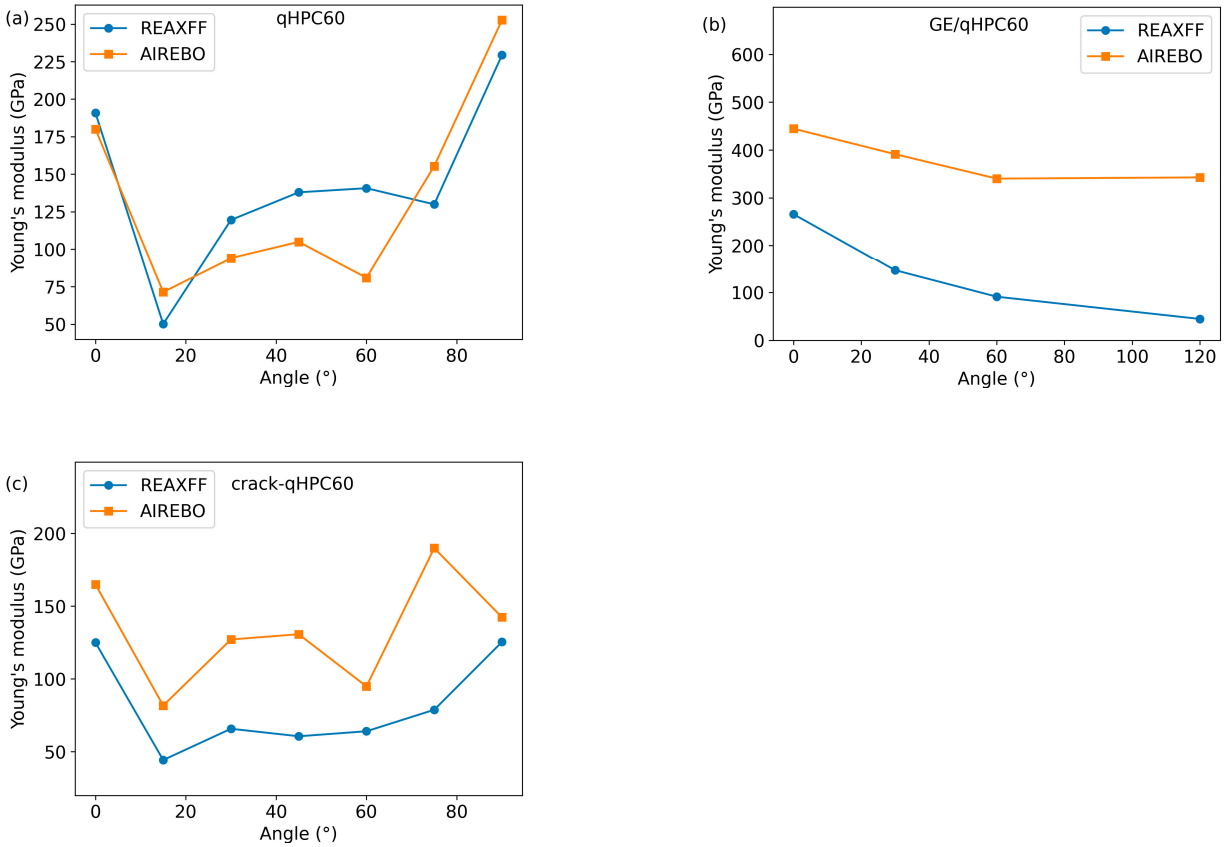

Figure 11. Relationship between Young's modulus and torsion angle of (**a**) qHPC$_{60}$, (**b**) GE/qHPC$_{60}$, and (**c**) crack-qHPC$_{60}$ system.

4. Conclusions

We have investigated the mechanical properties of fullerphene/graphene composites and compared them to those of 2D torsion-angle fullerphenes using molecular dynamics simulations. We assessed the mechanical properties of 2D torsion-angle fullerphene models with three different potential functions (REAXFF, TERSOFF, and AIREBO) and examined their fracture stress and fracture strain through tensile tests. The fracture strain and fracture stress of 2D torsion-angle fullerphenes exhibited similar trends across the different potential functions. Notably, the data values with the REAXFF potential were significantly lower than those with the AIREBO potential. The 90° torsion-angle model and the 0° torsion-angle model showed the highest fracture stresses for the two potential functions, approximately 80 GPa and 25 GPa, respectively.

We further investigated the effect of pre-cracks on the mechanical properties of 2D torsion-angle fullerphene models. The presence of cracks reduced the fracture stress and fracture strain of the models, indicating that pre-cracks weaken their mechanical properties. Interestingly, some models, such as the 75° torsion-angle model, exhibited tearing, and their stress–strain curves showed a quadratic decrease. Additionally, we added a graphene substrate to the 2D torsion-angle fullerphene and observed the fracture behavior after stretching. The results showed that both the fracture strain and fracture stress of the model increased significantly with the addition of the graphene substrate, indicating that the graphene substrate enhances the model's strength. During stretching, the fracture of graphene and fullerphene was not synchronized, with the fullerphene fracturing before the graphene, and the stress–strain curves exhibited a quadratic decrease.

The data from this study provide a valuable reference for the application and development of graphene and fullerphene and offer insights into the mechanical properties of 2D fullerphene, holding promising implications for future applications.

Author Contributions: Conceptualization, Q.P. and H.-K.T.; Methodology, T.Y., X.C., X.-J.C. and H.-K.T.; Software, M.H., X.C., X.-J.C. and T.Y.; Validation, M.H., T.Y., and Q.P.; Formal analysis, M.H. and T.Y.; Investigation, T.Y., Y.Z. and Q.P.; Resources, Y.Z., Q.P., and H.-K.T.; Data curation, M.H., Q.P. and H.-K.T.; Writing—original draft preparation, M.H. and T.Y.; Writing—review and editing, X.C., Y.Z., X.-J.C., Q.P. and H.-K.T.; Visualization, M.H.; Supervision, Q.P. and H.-K.T.; Project administration, Q.P., Y.Z. and H.-K.T.; Funding acquisition, X.C., Y.Z., X.-J.C., Q.P. and H.-K.T. All authors have read and agreed to the published version of the manuscript.

Funding: The authors would like to acknowledge the support provided by the Shenzhen Science and Technology Program (Grant No. KQTD20200820113045081), National Natural Science Foundation of China (Grant No. 12272378, 12204130), Strategic Priority Research Program of Chinese Academy of Sciences (Grant No. XDB0620103), High-level Innovation Research Institute Program of Guangdong Province (Grant No. 2020B0909010003), Shenzhen Start-Up Research Funds (Grant No. HA11409065), HITSZ Start-Up Funds (Grant No. X2022000), and Shenzhen Key Laboratory of Advanced Functional Carbon Materials Research and Comprehensive Application (Grant No. ZDSYS20220527171407017).

Data Availability Statement: The data presented in this study are available on request.

Conflicts of Interest: The authors declare no conflict of interest.

Appendix A

The potential function AIREBO is expressed as

$$E = \frac{1}{2}\sum_{i}\sum_{i\neq j}\left[E_{ij}^{\mathrm{REBO}} + E_{ij}^{\mathrm{L}} + \sum_{k\neq i,jl\neq i,j,k} E_{ijkl}^{\mathrm{tors}}\right]$$

E_{ij}^{REBO} consists of a repulsion term and an attraction term and depends on the bond order between the two atoms, which is related to the spacing between the two atoms and has the following analytical formula:

$$\overline{b}_{ij} = \frac{1}{2}\left[b_{ij}^{\sigma-\pi} + b_{ji}^{\sigma-\pi}\right] + b_{ij}^{\pi}.$$

$$b_{ij}^{\pi} = \Pi_{ij}^{\mathrm{RC}} + b_{ij}^{\mathrm{DH}}.$$

$$b_{ij}^{\sigma-\pi} = \left[1 + \sum_{k(\neq i,j)} f_{ik}^{c}(r_{ik})G\left(\cos\left(\theta_{ijk}\right)\right)\mathrm{e}^{\lambda_{ijk}} + P_{ij}\left(N_i^{\mathrm{C}}, N_i^{\mathrm{H}}\right)\right]^{-1/2}.$$

The first term, b_{ij}^{π}, describes the radical (R) and the conjugate bond (C), the second term describes the dihedral angle of C=C, and $b_{ij}^{\sigma-\pi}$ is the same as the bond-order expression for the rebo potential.

The total potential energy of REAXFF is expressed as follows:

$$E_{\mathrm{system}} = E_{\mathrm{bond}} + E_{\mathrm{val}} + E_{\mathrm{tors}} + E_{\mathrm{vdW}} + E_{\mathrm{Coulomb}} + E_{\mathrm{over}} + E_{\mathrm{specific}}$$

And its bond-order resolvent is more complex compared to the AIREBO potential and consists of three parts.

$$BO_{ij} = BO_{ij}^{\sigma} + BO_{ij}^{\pi} + BO_{ij}^{\pi\pi}$$

In addition to the REAXFF potential and the AIREBO potential, we also used the TERSOFF potential, but it performed poorly. The TERSOFF potential introduces a bond-order parameter to modify the attraction potential, while including the local geometry information of the atoms, thus including the bonding tendency into the potential, so that

configurations that bond easily correspond to larger values, and larger ones make the potential E smaller, thus making the system tend to form these configurations. It takes the form of

$$E = \sum_i E_i = \frac{1}{2} \sum_{i \neq j} V_{ij}$$

$$V_{ij} = f_C(r_{ij}) \left[a_{ij} f_R(r_{ij}) + b_{ij} f_A(r_{ij}) \right]$$

where f_C is the truncation function, f_R and f_A are the repulsive and attractive potentials, respectively, and a_{ij} and b_{ij} are their moderators. TERSOFF chose Morse potential as the form of f_R and f_A

$$f_R(r) = A \exp(-\lambda_1 r)$$

$$f_A(r) = -B \exp(-\lambda_2 r)$$

b_{ij} is of the form

$$b_{ij} = \left(1 + \beta^n \zeta_{ij}^n\right)^{-1/2n}$$

$$\zeta_{ij} = \sum_{k \neq i,j} f_C(r_{ik}) g\left(\theta_{ijk}\right) \exp\left[\lambda_3^3 \left(r_{ij} - r_{ik}\right)^3\right]$$

$$g(\theta) = 1 + c^2/d^2 - c^2/\left[d^2 + \left(h - \cos\theta\right)^2\right]$$

where i is the central atom, j is its to-be-bonded atom, and k is a third party that affects the chemical bond i-j. ζ_{ij} can be regarded as the effective coordination number of i but excluding j. It contains the truncation function f_C, the angular function $g(\theta)$, and the bond length difference $(r_{ij} - r_{ik})$ as a function.

In addition to the REAXFF and AIREBO potentials, we also used the TERSOFF potential function to describe the simulated system. The experimental results (shown in Figure A1) differ from the trends obtained in the tensile simulation of the system using the REAXFF potential functions. When using the REAXFF potentials, the GE/qHPC$_{60}$ composite structure first breaks the qHPC$_{60}$ layer and then the GE layer, with a flatter fracture curve. By contrast, when using the TERSOFF potential, the system first breaks the GE layer and then the qHPC$_{60}$ layer. During this time, the structure of the fullerene sphere is broken, and the spherical structure is pulled apart into chains of atoms of different lengths. These atomic chains have stresses on them and are stretched and broken one by one as the stretching process proceeds. This discontinuous fracture process causes the stress–strain curve profile to show multiple zigzags and drops.

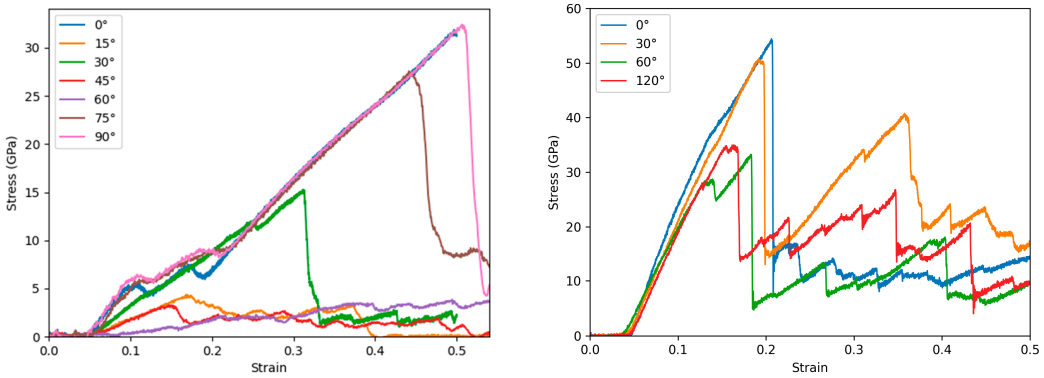

Figure A1. *Cont.*

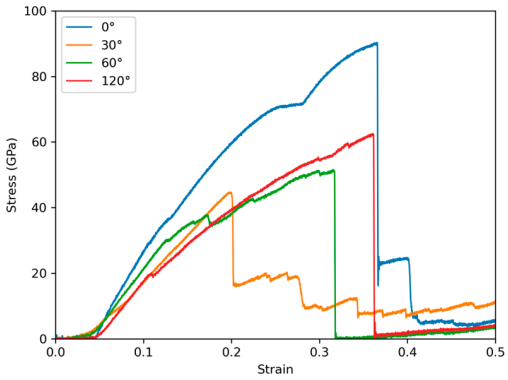

Figure A1. Stress–strain curves from tensile tests using the TERSOFF potential function for the $qHPC_{60}$ system (**top left**), the GE/$qHPC_{60}$ system without vacancies (**top right**), and the GE/$qHPC_{60}$ system with vacancies (**bottom left**).

Appendix B

There are two main steps in the model building; the first is to build the cornering cell, and the second is to extend each cornering cell to the same specification. Do the transformation of the original cell lattice vectors, through the linear combination of the original vectors, the appropriate combination coefficients are taken to obtain the new lattice vectors, and the angle between the two new vectors is transformed from the original angle to the target angle, as shown in Figure A2.

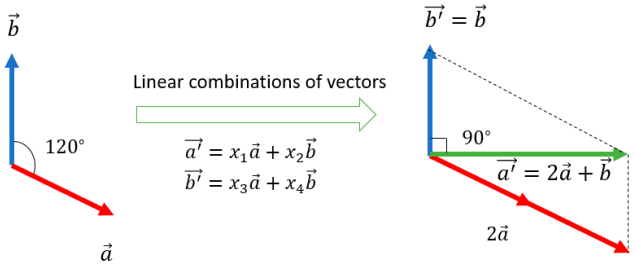

Figure A2. Transformations of the lattice vector.

It should be noted that taking the appropriate coefficients is a nonlinear integer programming problem, and three constraints need to be taken into account: the angle constraint (the value of the angle of the new vectors is a determinate); the right-hand-system constraint (the mixing product of the two vectors is greater than 0); and the integer constraint (the coefficients chosen are integers).

Original vectors are, as follows:

$$\vec{a}, \vec{b}$$

New vectors are, as follows:

$$\begin{aligned} \vec{a'} &= x_1\vec{a} + x_2\vec{b} = (a_1, a_2, a_3) \\ \vec{b'} &= x_3\vec{a} + x_4\vec{b} = (b_1, b_2, b_3) \end{aligned}$$

Three constraints are satisfied, as follows:

$$\cos\theta = \frac{(\vec{a}, \vec{b})}{|\vec{a}||\vec{b}|} = \frac{(a_1b_1 + a_2b_2 + a_3b_3)}{\sqrt{a_1^2 + a_2^2 + a_3^2}\sqrt{b_1^2 + b_2^2 + b_3^2}}$$

$$[X_1, X_2] = \begin{vmatrix} x_1 & x_2 \\ x_3 & x_4 \end{vmatrix} = x_1x_4 - x_2x_3 > 0$$

$$x_1, x_2, x_3, x_4 \in Z$$

The coefficients can be computed by a Python program that designs a solver for the optimization problem and finds the values of the variables that minimize the objective function by enumerating all possible combinations of variables in a given range. Then, the lattice by MS (Material Studio) is redefined to finally obtain the corner model cell for the specific angles we need.

Based on this, we need to expand these cells into supercells with the same specifications and then perform the tensile simulation. The process of cell expansion needs to pay attention to the periodicity of the supercells. Parts of the cells have a small number of atoms and can be adjusted within a certain realm; others have more atoms, even 1000, and the expansion of the number of atoms in these cells results in difficulty in controlling the number of atoms. We can solve this problem through a program. We need to specify a uniform size of model specification (e.g., around 10,000 atoms, or use area as a measure), and for cells with different angles, it is most convenient to set that standard as a common multiple of the area of all the cells. Then, it is necessary to calculate the expansion multiplier for each cell and set Replicate in OVITO to complete the expansion, as shown in Figure A3.

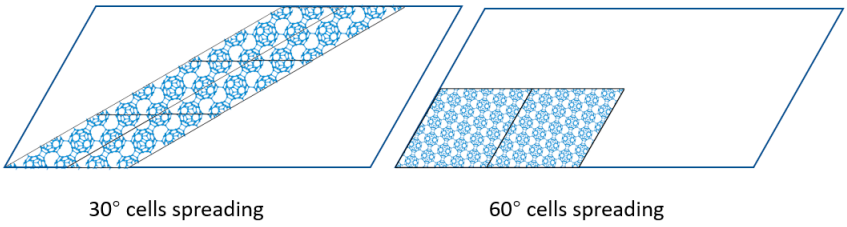

Figure A3. Schematic representation of different cells spreading.

Appendix C

Molecular sphere rupture and possible slight deformations can have an effect on the practical application of the material, so we need to focus on the volumetric strain of the material. The figures here are additions to the main text. Figure A4 shows the volumetric strain of the models before and after fracture, and Figure A5 shows the average stress and the stretch tensor of the xx component.

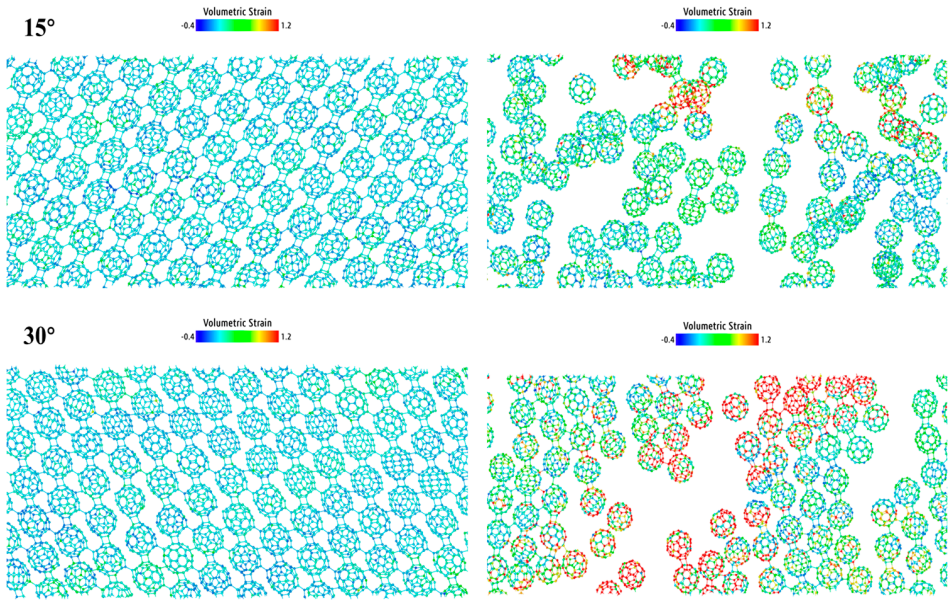

Figure A4. *Cont.*

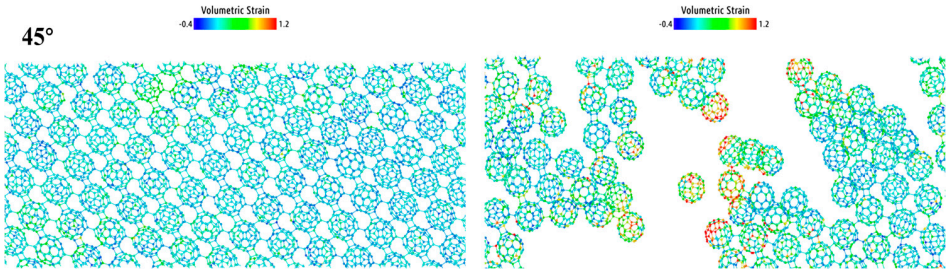

Figure A4. Volumetric strain images before fracture (**left**) and after fracture (**right**) of the 15°, 30°, and 45° models.

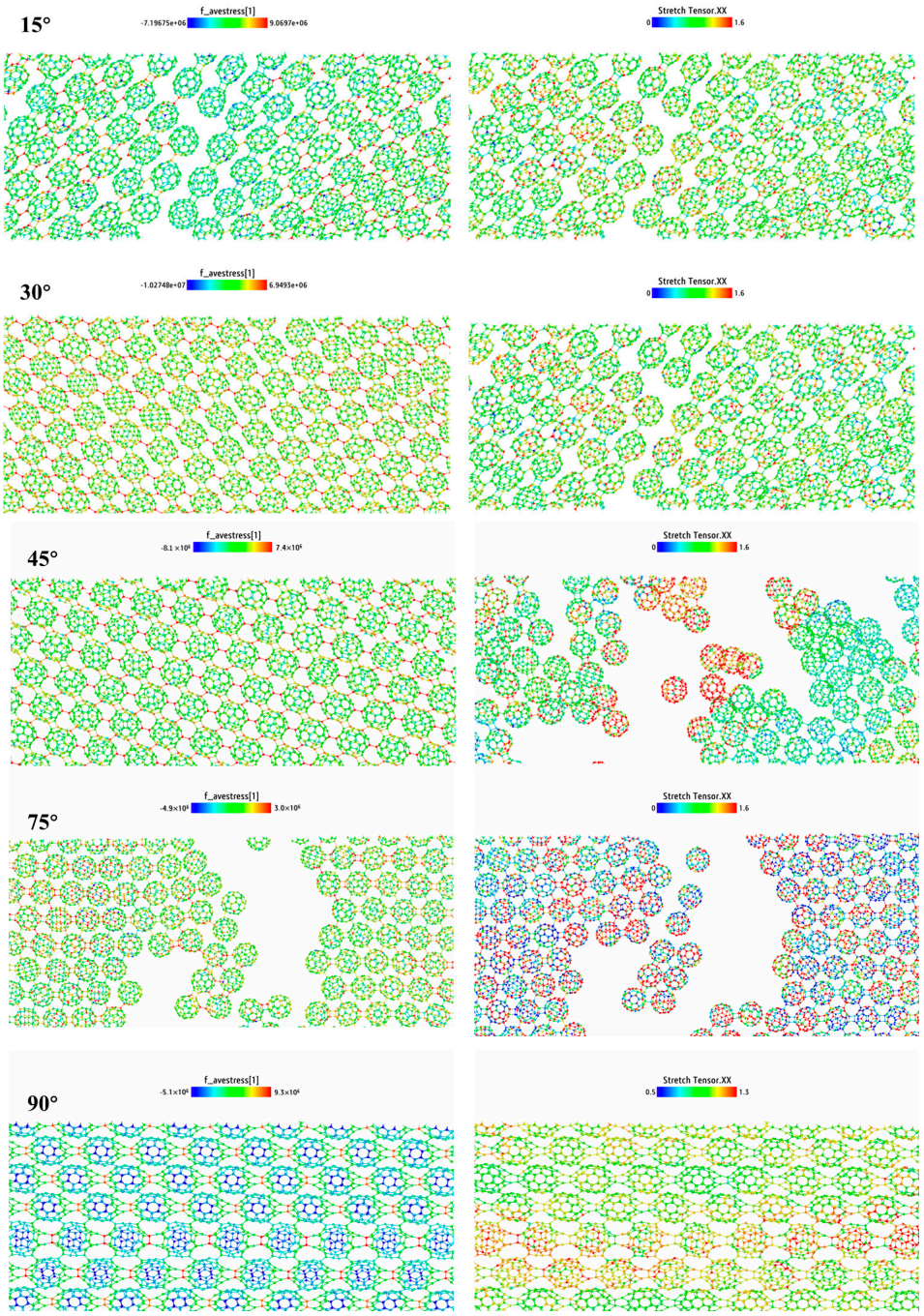

Figure A5. The XX component of the average stress (**left**) and the XX component of the stretch tensor (**right**) for the 0°, 15°, 30°, 45°, 75°, and 90° models.

Appendix D

Since experimental data are not yet available for the materials studied in this paper, we used several different potential functions to simulate the system and obtained results that show the same trend. This consistency demonstrates the reliability of our findings. Additionally, we compared our simulation results with those from other studies, as shown in the following table.

Table A1. Comparison of simulation results for several similar systems.

System	Potential Function	Fracture Stress (GPa)	Fracture Strain	Reference
$qHPC_{60}$ (0°)	REAXFF	26.85	0.11	Our work
	AIREBO	51.33	0.30	
GE/$qHPC_{60}$ (0°)	REAXFF	26.85	0.11	
	AIREBO	116	0.27	
$qHPC_{60}$ (0°)-crack	REAXFF	13.87	0.10	
	AIREBO	42.70	0.23	
$qHPC_{60}$	REAXFF	24.50	0.14	Nanomaterials 2023, 13, 1936 [17]
gp + $qHPC_{60}$ (0°)		39.5	0.26	
$qHPC_{60}$ (0°)-crack		17.3	0.12	
mC_{60}	/	1.10×10^{-08}	0.074	Carbon 202 (2023) 118–124 [18]

Appendix E

In this study, we conducted multiple repeated experiments to ensure the reliability and accuracy of our results. By performing statistical analysis on the data from all the experiments, we calculated the average stress–strain values and plotted the corresponding error bands. As illustrated in the graph, the average curve accurately reflects the common features of the experiments, while the error band represents the range of variability in the experimental results.

The error bands are relatively narrow, with variability being negligible before the fracture phase and only slightly increased at the fracture part. The overall error remains small, indicating low variability in the experimental data. This implies that our experiments are highly repeatable and reliable. In other words, any single experiment's result can approximately represent the overall reasonable outcome. This consistency further validates the stability and reliability of our experimental methods and conditions.

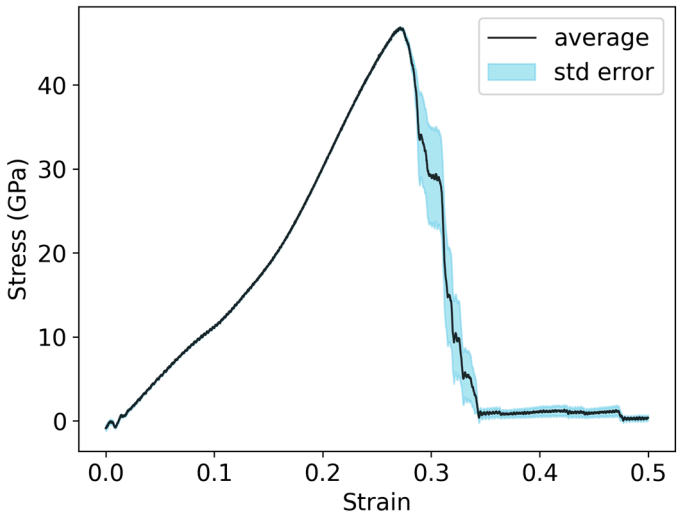

Figure A6. Average stress-strain curve and error bands.

References

1. Rao, C.N.R.; Biswas, K.; Subrahmanyam, K.S.; Govindaraj, A. Graphene, the New Nanocarbon. *J. Mater. Chem.* **2009**, *19*, 2457. [CrossRef]
2. García de Abajo, F.J. Graphene Plasmonics: Challenges and Opportunities. *ACS Photonics* **2014**, *1*, 135–152. [CrossRef]
3. Geim, A.K. Graphene: Status and Prospects. *Science* **2009**, *324*, 1530–1534. [CrossRef] [PubMed]
4. Tromer, R.M.; Ribeiro, L.A., Jr.; Galvão, D.S. A DFT Study of the Electronic, Optical, and Mechanical Properties of a Recently Synthesized Monolayer Fullerene Network. *Chem. Phys. Lett.* **2022**, *804*, 139925. [CrossRef]
5. Yu, L.; Xu, J.; Peng, B.; Qin, G.; Su, G. Anisotropic Optical, Mechanical, and Thermoelectric Properties of Two-Dimensional Fullerene Networks. *J. Phys. Chem. Lett.* **2022**, *13*, 11622–11629. [CrossRef]
6. Peng, B. Monolayer Fullerene Networks as Photocatalysts for Overall Water Splitting. *J. Am. Chem. Soc.* **2022**, *144*, 19921–19931. [CrossRef] [PubMed]
7. Dong, H.; Cao, C.; Ying, P.; Fan, Z.; Qian, P.; Su, Y. Anisotropic and High Thermal Conductivity in Monolayer Quasi-Hexagonal Fullerene: A Comparative Study against Bulk Phase Fullerene. *Int. J. Heat Mass Transf.* **2023**, *206*, 123943. [CrossRef]
8. Yuan, D.; Pi, H.; Jiang, Y.; Hu, Y.; Zhou, L.; Jia, Y.; Su, G.; Fang, Z.; Weng, H.; Ren, X. Highly In-Plane Anisotropic Optical Properties of Fullerene Monolayers. *Sci. China. Ser. G Phys. Mech. Astron.* **2023**, *66*, 247211. [CrossRef]
9. Ying, P.; Dong, H.; Liang, T.; Fan, Z.; Zhong, Z. Atomistic Insights into the Mechanical Anisotropy and Fragility of Monolayer Fullerene Networks Using Quantum Mechanical Calculations and Machine-Learning Molecular Dynamics Simulations. *Extrem. Mech. Lett.* **2023**, *58*, 101929.
10. Mortazavi, B. Structural, Electronic, Thermal and Mechanical Properties of C60-Based Fullerene Two-Dimensional Networks Explored by First-Principles and Machine Learning. *Carbon* **2023**, *213*, 118293. [CrossRef]
11. Mortazavi, B.; Shojaei, F.; Zhuang, X. A Novel Two-Dimensional C36 Fullerene Network; an Isotropic, Auxetic Semiconductor with Low Thermal Conductivity and Remarkable Stiffness. *Mater. Today Nano* **2023**, *21*, 100280. [CrossRef]
12. Liang, W.; Lu, G.; Yu, J. Machine Learning Accelerates Molten Salt Simulations: Thermal Conductivity of $MgCl_2$-NaCl Eutectic. *Adv. Theory Simul.* **2022**, *5*, 2200206. [CrossRef]
13. Mortazavi, B.; Novikov, I.S.; Podryabinkin, E.V.; Roche, S.; Rabczuk, T.; Shapeev, A.V.; Zhuang, X. Exploring Phononic Properties of Two-Dimensional Materials Using Machine Learning Interatomic Potentials. *Appl. Mater. Today* **2020**, *20*, 100685. [CrossRef]
14. Mortazavi, B.; Podryabinkin, E.V.; Novikov, I.S.; Roche, S.; Rabczuk, T.; Zhuang, X.; Shapeev, A.V. Efficient Machine-Learning Based Interatomic Potentialsfor Exploring Thermal Conductivity in Two-Dimensional Materials. *J. Phys. Mater.* **2020**, *3*, 02LT02. [CrossRef]
15. Mortazavi, B.; Shahrokhi, M.; Shojaei, F.; Rabczuk, T.; Zhuang, X.; Shapeev, A.V. A First-Principles and Machine-Learning Investigation on the Electronic, Photocatalytic, Mechanical and Heat Conduction Properties of Nanoporous C_5N Monolayers. *Nanoscale* **2022**, *14*, 4324–4333. [CrossRef] [PubMed]
16. Peng, B. Stability and Strength of Monolayer Polymeric C60. *Nano Lett.* **2023**, *23*, 652–658. [CrossRef] [PubMed]
17. Yu, T.; Li, J.; Han, M.; Zhang, Y.; Li, H.; Peng, Q.; Tang, H.-K. Enhancing the Mechanical Stability of 2D Fullerene with a Graphene Substrate and Encapsulation. *Nanomaterials* **2023**, *13*, 1936. [CrossRef] [PubMed]
18. Zhao, S.; Zhang, X.; Ni, Y.; Peng, Q.; Wei, Y. Anisotropic Mechanical Response of a 2D Covalently Bound Fullerene Lattice. *Carbon* **2023**, *202*, 118–124. [CrossRef]
19. Shen, G.; Li, L.; Tang, S.; Jin, J.; Chen, X.-J.; Peng, Q. Stability and Elasticity of Quasi-Hexagonal Fullerene Monolayer from First-Principles Study. *Crystals* **2023**, *13*, 224. [CrossRef]
20. Ribeiro, L.A., Jr.; Pereira, M.L., Jr.; Giozza, W.F.; Tromer, R.M.; Galvão, D.S. Thermal Stability and Fracture Patterns of a Recently Synthesized Monolayer Fullerene Network: A Reactive Molecular Dynamics Study. *Chem. Phys. Lett.* **2022**, *807*, 140075. [CrossRef]
21. Xue, Y.; Park, H.S.; Jiang, J.-W. On/off Switchable Interfacial Thermal Resistance in Graphene/Fullerene/Graphene Heterostructures. *Int. J. Heat Mass Transf.* **2023**, *212*, 124222. [CrossRef]
22. Plimpton, S. Fast Parallel Algorithms for Short-Range Molecular Dynamics. *J. Comput. Phys.* **1995**, *117*, 1–19. [CrossRef]
23. Stukowski, A. Visualization and Analysis of Atomistic Simulation Data with OVITO–the Open Visualization Tool. *Model. Simul. Mat. Sci. Eng.* **2010**, *18*, 015012. [CrossRef]
24. Stuart, S.J.; Tutein, A.B.; Harrison, J.A. A Reactive Potential for Hydrocarbons with Intermolecular Interactions. *J. Chem. Phys.* **2000**, *112*, 6472–6486. [CrossRef]
25. Senftle, T.P.; Hong, S.; Islam, M.M.; Kylasa, S.B.; Zheng, Y.; Shin, Y.K.; Junkermeier, C.; Engel-Herbert, R.; Janik, M.J.; Aktulga, H.M.; et al. The ReaxFF Reactive Force-Field: Development, Applications and Future Directions. *Npj Comput. Mater.* **2016**, *2*, 15011. [CrossRef]
26. Yang, X.; Wu, S.; Xu, J.; Cao, B.; To, A.C. Spurious Heat Conduction Behavior of Finite-Size Graphene Nanoribbon under Extreme Uniaxial Strain Caused by the AIREBO Potential. *Phys. E Low Dimens. Syst. Nanostruct.* **2018**, *96*, 46–53. [CrossRef]
27. Tersoff, J. New Empirical Approach for the Structure and Energy of Covalent Systems. *Phys. Rev. B Condens. Matter* **1988**, *37*, 6991–7000. [CrossRef] [PubMed]
28. Umeno, Y.; Yachi, Y.; Sato, M.; Shima, H. On the Atomistic Energetics of Carbon Nanotube Collapse from AIREBO Potential. *Physica E Low Dimens. Syst. Nanostruct.* **2019**, *106*, 319–325. [CrossRef]

29. Jensen, B.D.; Wise, K.E.; Odegard, G.M. Simulation of the Elastic and Ultimate Tensile Properties of Diamond, Graphene, Carbon Nanotubes, and Amorphous Carbon Using a Revised ReaxFF Parametrization. *J. Phys. Chem. A* **2015**, *119*, 9710–9721. [CrossRef]
30. van Duin, A.C.T.; Dasgupta, S.; Lorant, F.; Goddard, W.A. ReaxFF: A Reactive Force Field for Hydrocarbons. *J. Phys. Chem. A* **2001**, *105*, 9396–9409. [CrossRef]